Structural Analysis of Liquid Crystal Polymer Based Nanocomposites by X-Ray Scattering[a]

Jayita Bandyopadhyay, Suprakas Sinha Ray,* Mosto Bousmina

The main theme of this work is to support the unusual melt-state rheological properties of the clay-containing nanocomposites of thermotropic liquid crystal polymers by small- and wide-angle X-ray scattering. The changes of dispersion of silicate particles in the LCP matrix as well as change in crystal growth of LCP were extensively studied by X-ray scattering in both small- and wide-angle regions. The generalised indirect Fourier transformation technique developed by Glatter was used to study the structural changes in nanocomposites with temperature. This is a new approach recently proposed by us for the quantitative analysis of the nanoparticles dispersion in the polymer matrix.

The probability of finding neighbouring particles in the nanocomposite with the variation of clay concentration. Analysis done according to deconvolution theory.

Introduction

Over the last few years, much effort has been made to develop high-performance novel polymeric materials through the benefit of nanotechnology. One such niche area is polymer nanocomposite technology or more particularly clay-containing polymer nanocomposites because of the low volume ($\approx$5%) additions of layered silicate particles into the polymer matrix, which results in substantial property enhancements

J. Bandyopadhyay, S. Sinha Ray
DST/CSIR Nanotechnology Innovation Centre, National Centre for Nano-structured Materials, Council for Scientific and Industrial Research, Pretoria 0001, Republic of South Africa
E-mail: rsuprakas@csir.co.za
J. Bandyopadhyay, S. Sinha Ray, M. Bousmina
Department of Chemical Engineering, Laval University, Quebec, Canada G1K 7P4
S. S. Ray
Faculty of Natural and Agricultural Sciences, Department of Chemistry, University of the Free State (Qwaqwa Campus), Phuthaditjhaba 9866, Republic of South Africa
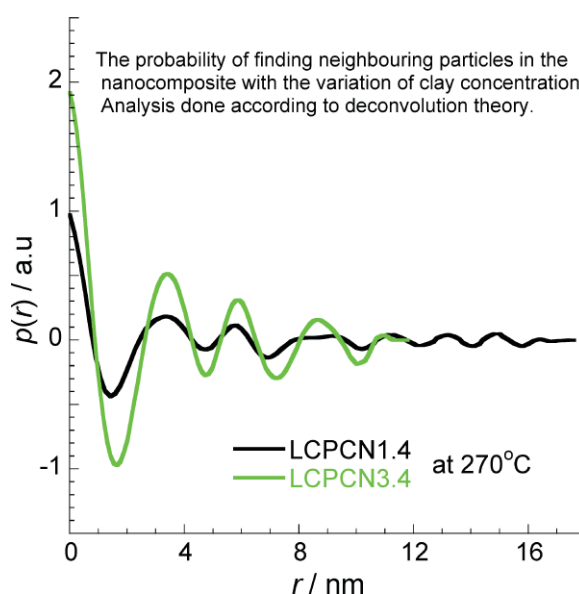
with respect to the neat polymer matrix.[1–7] The properties of such nanocomposites are directly related to the dispersion level of the clay particles in the polymer matrix and also on the orientation of the dispersed phase and the polymer chains itself. In the first article in this series, X-ray diffraction (XRD) patterns showed that the orientation of the liquid crystal polymer (LCP) changed after the addition of organoclay with different concentrations and the nanocomposites (LCPCNs) attained more ordered structures compared to the pure LCP.[8] Thus, it is possible to tune the orientation and ordering of LCP by adding the nano-filler. In the second article, we showed how the structures as well as the flow behaviour of the pure LCP and the LCPCNs changed under oscillatory shearing force.[9] The unique uplifting nature of both storage and loss moduli of LCP and its LCPCNs in the low frequency region during the frequency sweep was supported nicely by the two-dimensional (2D) small- and wide-angle X-ray scattering (SWAXS) patterns (see Supporting Information, Figure S2, and ref. [9]).

Macromol. Chem. Phys. **2010**, *211*, 1632–1639

1632 © 2010 WILEY-VCH Verlag GmbH & Co. KGaA, Weinheim

WILEY
InterScience®
DISCOVER SOMETHING GREAT

DOI: 10.1002/macp.201000016

Since in the case of nanocomposites, the crystal growth depends on the dispersion level of the filler material, it is therefore important to understand the dispersion characteristics of the silicate particles in the LCP matrix. Furthermore, LCP shows change in ordering in the system with the variation of temperature. Therefore, the objective of this work is to understand the structural/phase change of LCPCNs as a function of temperature by using the SWAXS technique.

Experimental Part

### Materials and Nanocomposite Preparation

The commercially available main chain thermotropic LCP, Vectra B950 used in this study was supplied by Ticona (USA). The organoclay used for the preparation of nanocomposites was dimethyl dehydrogenated tallow quaternary ammonium modified montmorillonite (MMT, commercially known as C20A, Southern Clay Products, USA). Figure 1a and b display the chemical formulas of Vectra B950 and the organic modifier used to modify the pure MMT. Nanocomposites with two different loadings of C20A were prepared by melt extrusion in a Haake twin-screw extruder at a screw speed of 30 rpm. The barrel temperatures used were 260, 270 and 270 °C, and the temperature of the capillary die was 270 °C. The samples (of thickness $\approx$90 µm) were moulded using a Carver laboratory press at 290 °C under 2 MPa pressure for 2 min, whereas the total moulding time was 12 min. The amount of the inorganic part present in the nanocomposite samples was determined by using a thermogravimetric analyser (TGA, Q500 TA Instrument). According to the TGA data (conducted under air), the amount of the inorganic part present in the first batch of nanocomposite sample was 1.4% and that in the second batch of nanocomposite sample was 3.4%. Therefore, the abbreviations used for these nanocomposites were LCPCN1.4 and LCPCN3.4, respectively. The thermal stability of C20A at the processing conditions was also measured by TGA. Details can be found in our previous article.[8]

Structural Characterisation by SWAXS

The SWAXS analyses were carried out by an Anton Paar SAXSess instrument, operated at 40 kV and 50 mA with a line collimation

(a)

(b)

(HT: ~65% C18, ~30% C16, ~5% C14)
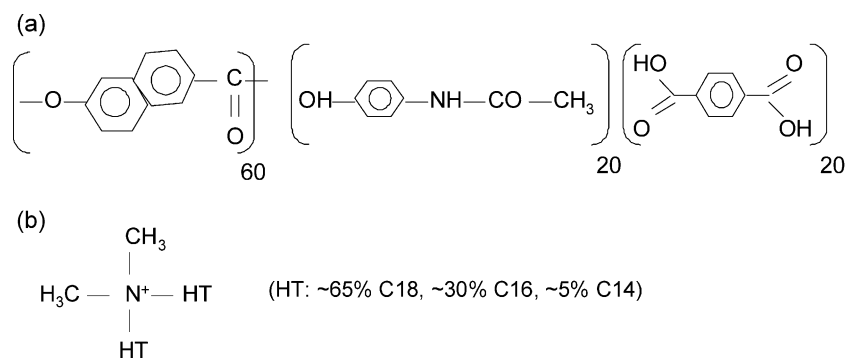
Figure 1. (a) Molecular structure of Vectra B950 and (b) the chemical structure of surfactant used to modify pure MMT.
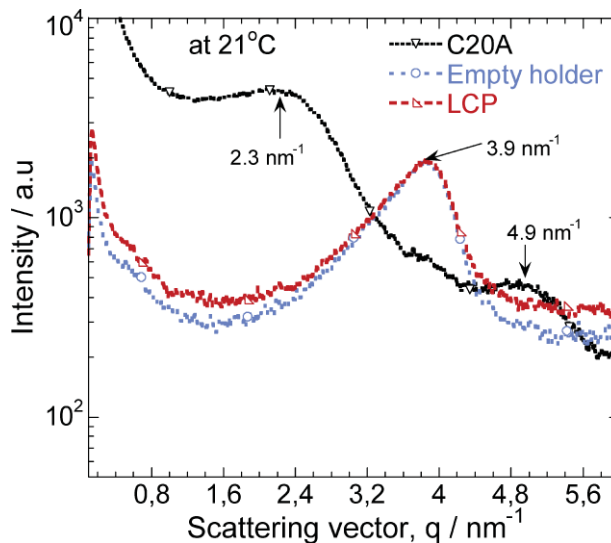
Figure 2. X-ray scattering patterns (without normalisation) of pure LCP, empty sample holder (paste cell) and pure C30B powder in the small-angle (SAXS) region. The compression moulded sheet of pure LCP and empty sample holder were exposed under X-ray for 1 min and the pure C20A powder for 10 s.

geometry. The radiation used was a Ni-filtered Cu K$_\alpha$ radiation of wavelength 0.154 nm (PAN Analytical). Intensity profiles were obtained with a slit collimated SAXSess and recorded with a 2D imaging plate. Sample to detector distance was 264.5 mm and covers the length of the scattering vector (q) from 0.13 to 28 nm^{-1}. The read-out angles were calculated from the pixel size and the obtained q-scale was cross-checked by measuring silver behenate whose equidistant peak positions are known. The thin sheet (thickness $\approx$90 µm) of LCP and LCPCNs were heated in a paste cell from the room temperature to 280 °C in successive steps and then cooled down to the room temperature by a TCU50 (Anton-Paar) temperature control unit, which is attached to the SAXSess instrument. SWAXS data of pure LCP and LCPCNs were collected at temperatures of 21, 250, 270 and 280 °C during heating and after cooling at 21 °C. According to the DSC results, all samples possess three melting peaks along with the re-crystallisation (i.e. increase in ordering in the system) between the melting peaks.[8] We selected three temperatures in such a way that we can see some effect of phase transitions: just before first melting (250 °C), in between first and second melting where there is increase in ordering in the system (270 °C) and after second melting (280 °C). These samples were kept at the above-mentioned temperatures for 5 min including 1 min exposure time under X-ray irradiation. In order to avoid the forward scattering, the pure C20A clay was exposed under X-ray irradiation for 10 s at room temperature. The empty sample holder was also exposed under X-ray for 1 min at room temperature.

Results and Discussion

Small-angle X-ray scattering (SAXS) is a powerful tool used to determine the size, shape and internal structure of the particle system of sizes ranging from 1 to 100 nm. SAXS analysis is mainly applicable for randomly oriented and statistically distributed particle systems. Hence, their three-dimensional (3D) scattering pattern represents the orientational average of their structure. Only in the case of three types of ideal symmetry; i.e. for spherical, cylindrical and lamellar structures with a centrosymmetric scattering length density distribution, there is no loss of information due to the orientational averaging.[10] Now this orientational averaging is radially symmetric and can therefore be reduced to the 1D angle-dependent scattering intensity function $I(q)$,

$$I(q) = 4\pi \int_0^\alpha p(r) \frac{\sin qr}{qr} dr \quad (1)$$

where q is the scattering vector and can be related to the scattering angle (θ) and wavelength (λ) through

$$q = \frac{4\pi}{\lambda} \sin \theta \quad (2)$$

$p(r)$ in Equation (1) represents a pair distance distribution function of the electrons; or in other words, the radial or spherical symmetric correlation function of electron density differences weighted by $4\pi r^2$. It shows directly the probability of finding a pair of electron densities at a particular distance r. All the information available from the experimental curves in the small-angle region is in reciprocal space since $q \propto 1/\lambda$.

It is also well known that SAXS is a useful tool to determine the dispersion level of clay layers in the nanocomposites. Figure 2 shows the SAXS pattern of compression-moulded film of pure LCP, C20A powder and empty sample holder (paste cell) at room temperature. Because of crystalline layered structure, in the SAXS region the 1st order basal reflection of C20A powder appeared at $\approx$2.3 nm^{-1}. The 2nd order basal reflection of C20A appeared at almost twice this q value

($\approx$4.9 nm^{-1}). The sharp peak at $\approx$3.9 nm^{-1} appeared for the pure LCP and the empty holder is due to the kapton film window of the paste cell.

Generally, the SWAXS data contain information contributed by both the polymer and the dispersed silicate layers.[11] To understand the structure of the dispersed clay layers in the LCPCNs, first LCP (at different temperatures) was taken as a background and then subtracted from the
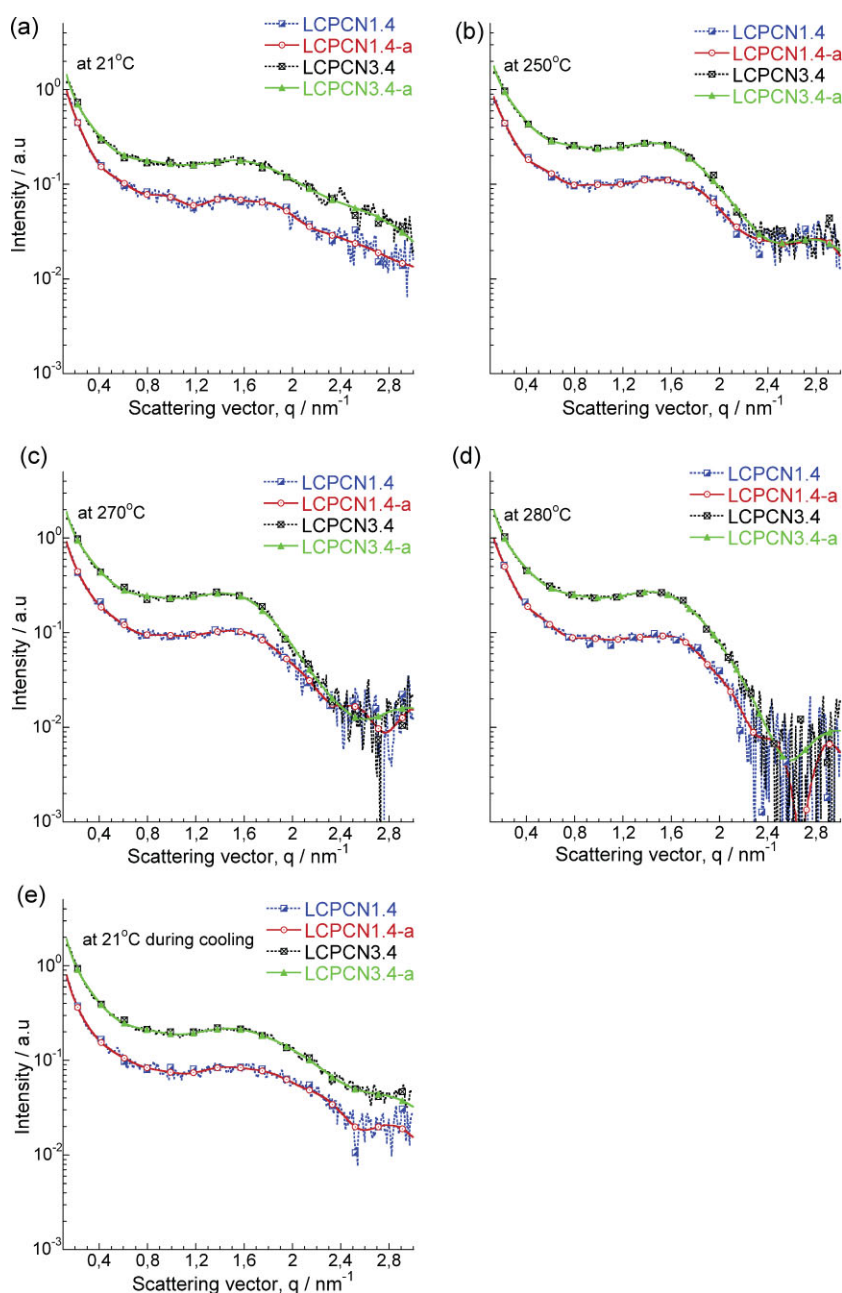

Figure 3. Background (scattering from pure LCP) and Porod subtracted scattering curves of LCPCNs in the small-angle region showing the effect of temperature on the dispersion characteristics of organoclay in the polymer matrix. The dotted and solid patterns represent, respectively, the experimental and approximated (according to GIFT) scattering curves: (a) 21, (b) 250, (c) 270, (d) 280 and (e) 21 °C during cooling.

scaled intensity (without normalisation) versus q curves for the nanocomposites at corresponding temperatures. Finally, after Porod extrapolation, the constant background was subtracted and the results are presented by the dotted patterns in the different parts of Figure 3. According to Figure 3, a less intense crystalline clay peak appeared at $q = 1.6 \, nm^{-1}$ in the SAXS patterns of both LCPCNs at 21 °C. This peak corresponds to the scattering from the (001) plane of the dispersed clay particles in the LCP matrix. With the variation of temperature, although the shape of the scattering pattern changes a bit, the peak positions remain almost the same. At a higher temperature, the peaks become more pronounced and during cooling at 21 °C the curves attain again almost their initial shapes. This phenomenon becomes more noticeable as the clay loading increases. Due to the intercalation of polymer chains in the clay galleries, the lamellar structure of C20A swells. According to the reciprocity theorem of scattering, those swallowed structures of lamellar C20A then scatters in the small angle compared to pure C20A, and, hence, the clay peak in the nanocomposites shift towards the lower angle side. As already described in the theory part, the degree of dispersion of silicate layers of clay particles in the polymer matrix can be considered as the thickness cross-section profile.

Now, all information available from the experimental curves in the small angle region are in reciprocal space. The real space transformation of the SAXS data was carried out according to the generalised indirect Fourier transformation (GIFT) method, discussed in the theoretical section (see Supporting Information). The scattering curves represented in Figure 3 without any extension stands for the experimental scattering curves after Porod subtraction and with extension '-a' stands for the theoretical scattering curves estimated according to the GIFT method. Figure 3 shows that the theoretical scattering curves coincide nicely with the experimental scattering curves. Therefore, $p(r)$ functions representing the theoretical scattering curves should be the same as for the experimental curves. The $p(r)$ of various LCPCNs is presented in Figure 4. The regions with opposite signs of different electron density give negative contributions to $p(r)$,

i.e. $p(r)$ can be negative in some regions as observed in Figure 4.[12] The exponentially decaying part of $p(r)$ first drops to zero; represents the usual single particle form factor, as well as the largest single particle dimension. The other peaks can be explained as first, second, third and so on correlation maxima. These correlation maxima represent the average radial distance to the next neighbouring domain, commonly known as long spacing.[13] When the two contributions overlap, i.e. the neighbours overlap, the peaks do not possess a tail; rather, curve shows a maximum and minimum. So according to Figure 4, there is almost no
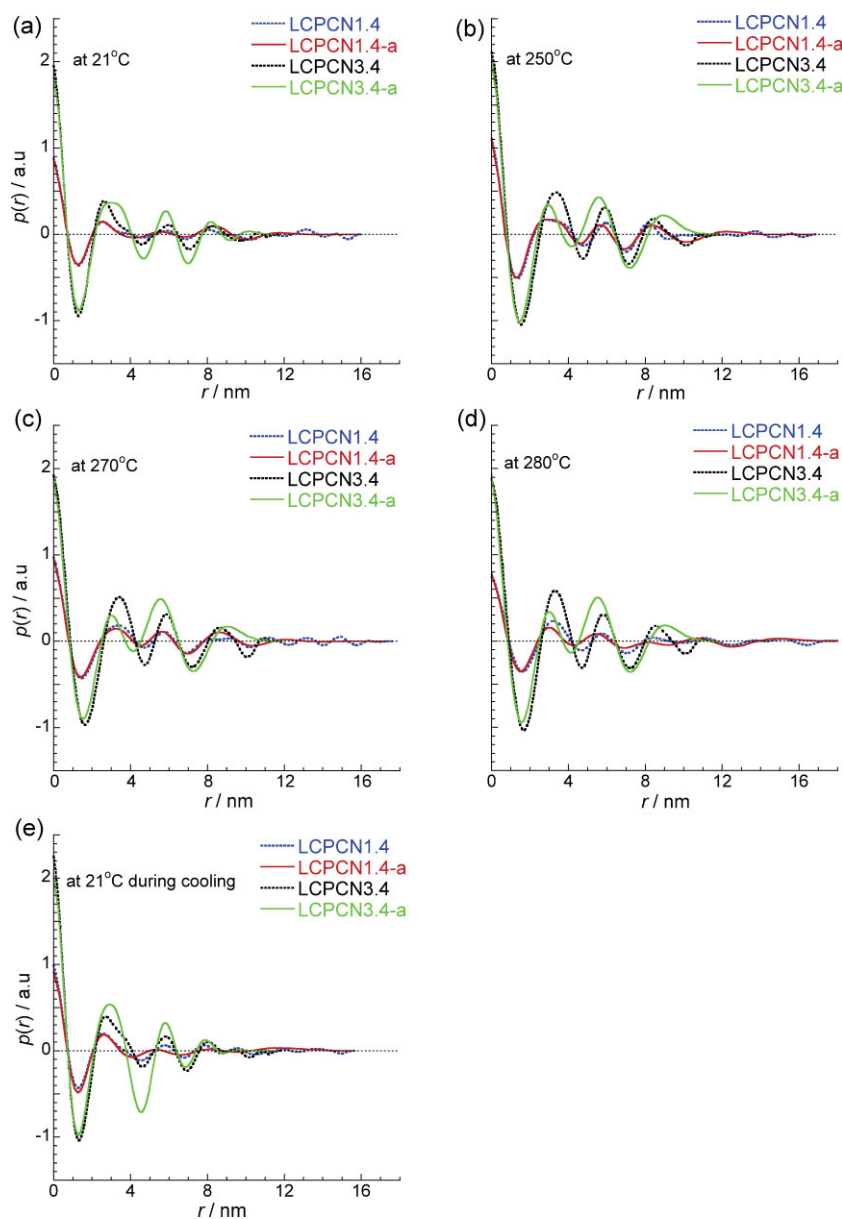
Figure 4. $p(r)$ for nanocomposites showing the probability of finding neighbouring particles in the LCPCNs with variation in clay concentration and temperature. The dotted and solid lines represent, respectively, the analyses according to GIFT and DECON (deconvolution): (a) 21, (b) 250, (c) 270, (d) 280 and (e) 21 °C during cooling.
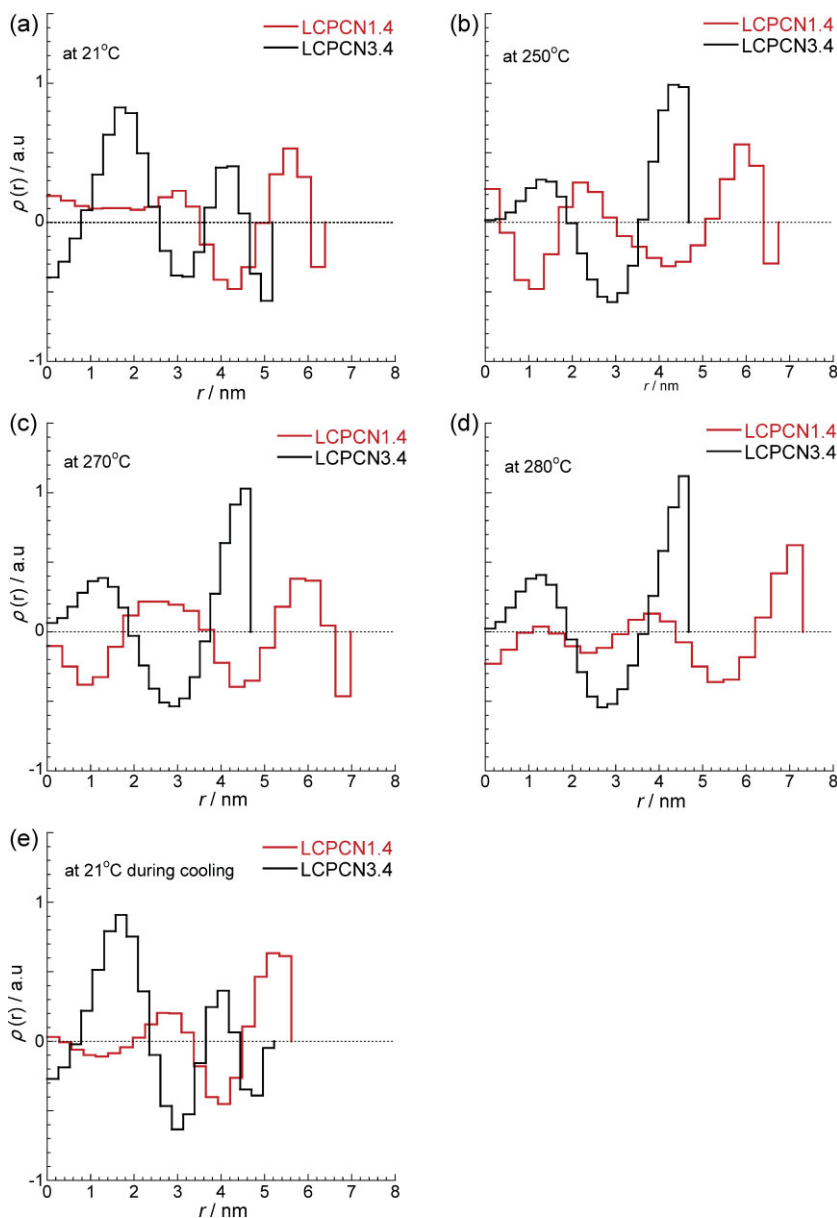
influence of C20A loading on the largest single particle size. With increase in temperature, the largest single particle dimension changes slightly from 0.7 (at 21 °C) to 0.95 nm (at 280 °C). During cooling up to room temperature this dimension attains again its initial value. Therefore, this small change can be considered as a result of thermal expansion.

To determine $p(r)$, the probable maximum distance of finding neighbour (D_{max}) estimated by GIFT is tabulated in Table 1. The deconvolution of this $p(r)$ (determined by GIFT) by DECON (deconvolution) software provides electron density distribution (of the thickness cross-section) profile. But, DECON needs to assume the amount of polydispersity (PD) present in the samples in order to get the similar $p(r)$ as determined by GIFT. Then only it is possible to confirm that the electron density distribution (of the thickness cross-

section) profile determined by DECON corresponds to the $p(r)$ determined by GIFT. The PD values and the positions of the correlation peaks determined by GIFT (r_{GIFT}) and DECON (r_{DECON}) for LCPCNs at different temperatures are also tabulated in Table 1. At room temperature (21 °C), in LCPCN1.4 and LCPCN3.4, the appearance of four correlation maxima indicate the presence of four neighbours, each possessing some portions that are overlapping each other within the maximum distance (D_{max}) of 16.1 and 11.7 nm, respectively. According to the r_{GIFT} or r_{DECON} value in Table 1 at 21 °C; although the probability of finding first three neighbours in both LCPCNs are almost the same, the probable distance of finding fourth neighbour in the case of LCPCN1.4 is larger than LCPCN3.4. This indicates that in the case of LCPCN1.4 the clay platelets are dispersed nicely compared to the LCPCN3.4. With increase in temperature up

Table 1. Parameters determined from the analysis carried out on the basis of GIFT and DECON.

Temperature	LCPCN1.4		LCPCN3.4		Number of correlation peaks	LCPCN1.4		LCPCN3.4	
°C	D_{max} nm	PD %	D_{max} nm	PD %		r_{GIFT} nm	r_{DECON} nm	r_{GIFT} nm	r_{DECON} nm
21	16.1	10	11.7	5	1	2.6	2.6	2.6	3.0
					2	5.8	5.6	5.9	5.9
					3	8.0	8.4	8.2	8.2
					4	13.0	11.9	10.7	10.2
250	16.99	10	11.8	10	1	3.0	3.0	3.4	3.0
					2	5.9	5.7	5.9	5.6
					3	8.1	8.4	8.4	8.9
					4	13.6	12.4		
270	17.6	10	11.8	10	1	3.3	3.3	3.4	3.0
					2	5.8	5.7	5.9	5.5
					3	8.6	8.7	8.6	9.0
					4	11.1	12		
					5	13.1			
					6	14.9			
280	18.4	10	11.8	10	1	3.2	3.0	3.3	3.0
					2	5.7	5.4	5.8	5.6
					3	8.3	(8.2)	8.5	9.0
					4	11.1	10.8		
					5	15.0	14.9		
21 (during cooling)	15.7	15	11.8	5	1	2.6	2.7	2.7	2.9
					2	5.7	5.3	5.8	5.8
					3	7.9	8.2	8.3	7.9
					4	9.5		10.7	9.7
					5	11.9	11.7		
					6	13.8			

Figure 5. Temperature dependence of electron density profile of the thickness cross-section in the LCPCNs: (a) 21, (b) 250, (c) 270, (d) 280 and (e) 21 °C during cooling.

has shown in Figure 4 and Table 1. In table, the third correlation peak is kept in bracket because of the presence of separate clay stacking in this position is a bit doubtful according to Figure 4. Again, in the case of LCPCN3.4, there is no significant change in distribution of clay particles since the correlation peaks appeared almost at the same distances like 270 °C. The cooling from melt (at 21 °C during cooling) brings back their initial structures. So, after this discussion it is clear that the intercalation of the polymer chains in the clay gallery is much stable in LCPCN3.4 compared to LCPCN1.4. Since D_{max} of LCPCN1.4 remains always higher than LCPCN3.4 (see Table 1), it can be inferred that LCPCN1.4 possesses slightly better delamination of clay layers compared to the other nanocomposite LCPCN3.4.

The deconvolution of the $p(r)$ function provides an electron density profile of the thickness cross-section as presented in Figure 5. According to Figure 5 and Table 2, LCPCNs have a fuzzy particle structure. When the clay platelets start peeling apart from each other in nanocomposites due to the intercalation of the polymer chains in the clay gallery, these fuzzy structures start to grow. Figure 5 and Table 2 show how the fuzzy layers represented by positive (+ve) and negative (−ve) electron density are varying with the temperature in LCPCNs. Initially LCPCN1.4 has four-layered fuzzy structure. As the temperature increases to 250 °C; the first layer (considered as the centre of the fuzzy structure) gets separated into three layers and the thickness of the three outer layers also changes. Any further variation of temperature results mainly change in central fuzzy structure compared to the three outer layers. For LCPCN3.4 electron density profile contains five layers at 21 °C, the first and last −ve electron density regions vanish at higher temperatures (250–280 °C) and reforms during cooling at 21 °C. Therefore, from this change of electron density profile of the thickness cross-section it can be confirmed that the intercalation of polymer chains in the clay gallery is much stable in LCPCN3.4 compared to LCPCN1.4. Now since LCPCN1.4 possesses less stable and comparatively better delaminated clay layers especially in the molten state (≥270 °C), it is then easy to align those stacked clay layers under shearing force.

to 250 °C, the probability of finding neighbours in LCPCN1.4 remains unaffected. But the number of neighbours reduces in the case of LCPCN3.4. At 270 °C, although GIFT shows some ripple at $r_{GIFT} = 11.1$ and 14.9 nm, according to the DECON still four clear correlation maxima are present in LCPCN1.4. For LCPCN3.4 three prominent correlation peaks are present at 270 °C as reported by r_{GIFT} and r_{DECON} in Table 1. The correlation peak positions remain the same in both LCPCNs when compared with the previous temperature. With increase in temperature to 280 °C, the probability of finding neighbouring particle increases in LCPCN1.4 as

Table 2. The fuzzy layers represented by positive (+ve) and negative (−ve) electron density (see Figure 6) are varying with the temperature in LCPCNs.

Sample	Temperature/°C	Electron density (−ve)	Electron density (+ve)	Electron density (−ve)	Electron density (+ve)	Electron density (−ve)	Electron density (+ve)	Electron density (−ve)	Electron density (+ve)	Electron density (−ve)
LCPCN1.4	21		$(2 \times 3.5) = 7.0$					$(2 \times 1.6) = 3.2$	$(2 \times 0.9) = 1.8$	$(2 \times 0.4) = 0.8$
	250		$(2 \times 0.3) = 0.6$	$(2 \times 1.4) = 2.8$	$(2 \times 1.3) = 2.6$			$(2 \times 2.1) = 4.2$	$(2 \times 1.3) = 2.6$	$(2 \times 0.3) = 0.6$
	270			$(2 \times 1.8) = 3.6$	$(2 \times 2) = 4.0$			$(2 \times 1.4) = 2.8$	$(2 \times 1.4) = 2.8$	$(2 \times 0.4) = 0.8$
	280			$(2 \times 1.1) = 2.2$	$(2 \times 0.3) = 0.6$	$(2 \times 1.9) = 3.8$	$(2 \times 1.1) = 2.2$	$(2 \times 1.8) = 3.6$	$(2 \times 1.1) = 2.2$	
	21-cool		$(2 \times 0.3) = 0.6$	$(2 \times 1.7) = 3.4$	$(2 \times 1.4) = 2.8$			$(2 \times 1.1) = 2.2$	$(2 \times 1.1) = 2.2$	
LCPCN3.4	21	$(2 \times 0.8) = 1.6$	$(2 \times 1.8) = 3.6$	$(2 \times 1) = 2.0$	$(2 \times 1.1) = 2.2$	$(2 \times 0.5) = 1.0$				
	250		$(2 \times 1.9) = 3.8$	$(2 \times 1.6) = 3.2$	$(2 \times 1.2) = 2.4$					
	270		$(2 \times 1.9) = 3.8$	$(2 \times 1.9) = 3.8$	$(2 \times 0.9) = 1.8$					
	280		$(2 \times 1.9) = 3.8$	$(2 \times 1.9) = 3.8$	$(2 \times 0.9) = 1.8$					
	21-cool	$(2 \times 0.8) = 1.6$	$(2 \times 1.6) = 3.2$	$(2 \times 1.3) = 2.6$	$(2 \times 0.7) = 1.4$	$(2 \times 0.8) = 1.6$				
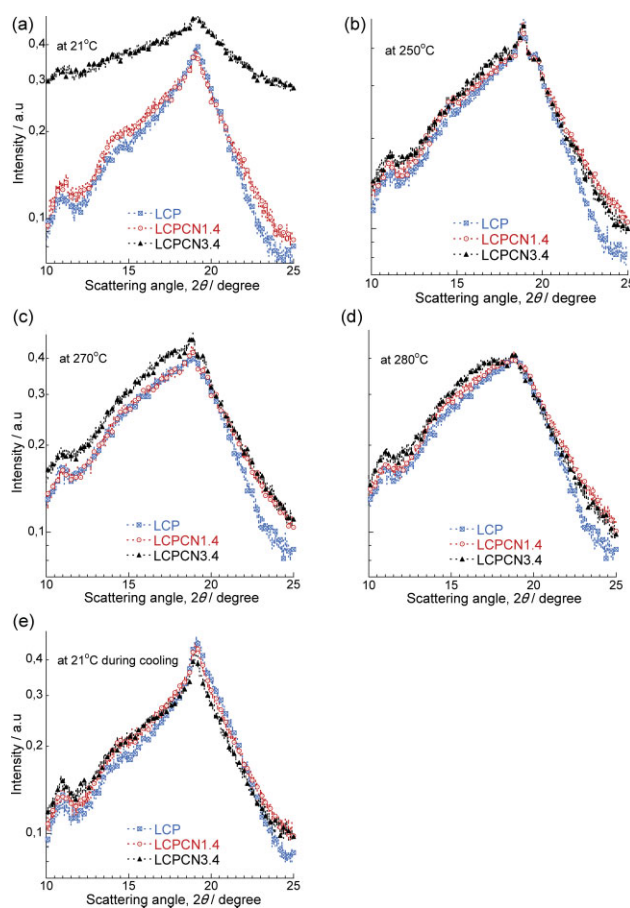
Figure 6. The scattering patterns (without normalisation) of pure LCP and LCPCNs in the wide-angle region are showing the modification of crystals with the variation of temperature: (a) 21, (b) 250, (c) 270, (d) 280 and (e) 21 °C during cooling.

The scattering patterns (without normalisation) of pure LCP and LCPCNs in the wide-angle region at different temperatures are presented in Figure 6. According to this figure, for all samples, the crystalline peak appeared at ≈19°. With increase in temperature to 250 °C, a new crystal peak appeared at ≈19.7° accompanied with the peak at ≈19°. This new crystal peak is may be due to the different form of the crystals. The growth of this crystal is not unusual, since for LCP it is expected that ordering in the system can increase in the course of heating. During melting at ≈270 °C, LCPCNs possesses contribution of amorphous (crystals already melted) and crystalline portions. But LCP maintains its' sharp peak even at 280 °C. Therefore, the crystallinity of the nanocomposites reduces slightly compared to the pure LCP.

Conclusion

In our first article, we showed that the orientation of LCP crystals changed the direction after nanocomposites formation with organoclay. Furthermore, according to the 2D SWAXS images, in the WAXS region crystallinity reduces with the increase in clay loading. Then from the above discussion in this article it is clear that the crystallinity decreases in LCPCN3.4. Again, since LCPCN3.4 possesses much stable intercalated structure it is difficult to orient the stacked clay layers by shear force as compared to LCPCN1.4. For this reason, under oscillatory shear force during frequency sweep, in the low frequency region (where structures get enough time to align themselves in the shear direction) uplifting nature of the storage and loss

modulus become less pronounced with increase in clay content (see Figure S2 in the Supporting Information).

[1] [1a] S. Sinha Ray, M. Okamoto, *Prog. Polym. Sci.* **2003**, *28*, 1539; [1b] S. Pavlidou, C. D. Papaspyrides, *Prog. Polym. Sci.* **2008**, *33*, 1119.

[2] [2a] F. F. Fang, H. J. Choi, J. Joo, *J. Nanosci. Nanotechnol.* **2008**, *8*, 1559; [2b] C. H. Lee, H. B. Kim, S. T. Lim, H. S. Kim, Y. K. Kwon, H. J. Choi, *Macromol. Chem. Phys.* **2006**, *207*, 444; [2c] K. Y. Mya, K. Wang, L. Chen, T. T. Lin, P. K. Pallathadka, J. Pan, C. He, *Macromol. Chem. Phys.* **2008**, *209*, 643.

[3] M. S. Osman, V. Mittal, U. W. Suter, *Macromol. Chem. Phys.* **2008**, *208*, 68.

[4] [4a] P. Maiti, P. J. P. Yadav, *J. Nanosci. Nanotechnol.* **2008**, *8*, 1858; [4b] D. Shah, P. Maiti, D. D. Jiang, C. A. Batt, E. P. Giannelis, *Adv. Mater.* **2005**, *17*, 525.

[5] [5a] S. Sinha Ray, M. E. Makhatha, *Polymer* **2009**, *50*, 4635; [5b] D. R. Paul, *Polymer* **2008**, *49*, 3187.

[6] S. Sinha Ray, K. Yamada, A. Ogami, M. Oakmoto, K. Ueda, *Nano Lett.* **2002**, *2*, 1093.

[7] [7a] C. E. Powell, G. W. Bell, *Curr. Opin. Solid State Mater.* **2006**, *35*, 3104; [7b] Y. H. Hyun, S. T. Lim, H. J. Choi, M. S. John, *Macromolecules* **2001**, *34*, 8084.

[8] J. Bandyopadhyay, S. Sinha Ray, M. Bousmina, *Macromol. Chem. Phys.* **2007**, *208*, 1979.

[9] J. Bandyopadhyay, S. Sinha Ray, M. Bousmina, *Macromol. Chem. Phys.* **2009**, *210*, 161.

[10] [10a] J. Bandyopadhyay, S. Sinha Ray, *Polymer* **2010**, *51*, 1437; [10b] R. Mittelbach, O. Glatter, *J. Appl. Crystallogr.* **1998**, *31*, 600.

[11] D. M. Lincoln, R. A. Vaia, Z. G. Wang, B. S. Hsiao, *Polymer* **2001**, *42*, 1621.

[12] H. Schnablegger, Y. Singh, *A Practical Guide to Small Angle X-Ray Scattering*, Anton Paar GmbH, Austria 2006.

[13] O. Glatter, O. Kratky, *Small Angle X-Ray Scattering*, Academic Press, London 1982.